Early Holocene sea-level changes along the western Bohai Sea coast
Far-field response to meltwater pulses

Tian, Lizhu; Vermeersen, Bert L.; Li, Jianfen; Wang, Hong; Wang, Fu

DOI
10.1016/j.quascirev.2025.109430

Publication date
2025

Document Version
Final published version

Published in
Quaternary Science Reviews

Quaternary Science Reviews 362 (2025) 109430

Contents lists available at ScienceDirect

Quaternary Science Reviews

journal homepage: www.elsevier.com/locate/quascirev

Early Holocene sea-level changes along the western Bohai Sea coast: Far-field response to meltwater pulses

Lizhu Tian [a,b], Bert L. Vermeersen [b,c], Jianfen Li [a], Hong Wang [a], Fu Wang [a,*]

[a] Tianjin Center (North China Center of Geoscience Innovation), China Geological Survey (CGS), CGS Key Laboratory of Coast Geo-Environment and Tianjin Key Laboratory of Coast Geological Processes and Environmental Safety, Tianjin, 300170, China
[b] Department of Estuarine and Delta Systems, NIOZ Royal Netherlands Institute for Sea Research, Yerseke, the Netherlands
[c] Faculty of Civil Engineering and Geosciences, TU Delft, Delft, the Netherlands

ARTICLE INFO

Handling Editor: Dr Mira Matthews

Keywords:
Melt water pulse
Early Holocene
Sea-level change
8.2 ka event
Bohai sea

ABSTRACT

Meltwater Pulses (MWPs) from the last deglaciation are highly relevant today. Studying their timing and characteristics offers valuable insights into past periods of accelerated sea-level response under intense climate forcing and provides an analog for potential future scenarios. The western Bohai Sea coast (WBSC), located deep within the Asian continent and far from major glaciation centers and subduction zones, exhibits sensitive relative sea level (RSL) responses to any high latitude ice-sheet meltwater influx, offering valuable data to refine the chronology and magnitude of MWPs. This paper presents 25 high-confidence early Holocene sea-level index points (SLIPs) from high marsh vegetation samples, generated through analysis of sediments, microfossil foraminifera, and radiocarbon dating of 14 cores from the WBSC. The altitudes of SLIPs were adjusted for factors such as self-compaction, long-term tectonic subsidence, and ground lowering due to water extraction. The early Holocene RSL history in the WBSC reflects a rapid rise in sea level during ~9800–6900 cal a BP, occurring within the global context of global sea-level rise. During ~9800–8100 cal a BP, the RSL rise was faster, averaging 7–8 mm/a, characterized by two distinct stepwise increases. A rapid sea-level rise event before 9500 cal a BP was shown by a sharp RSL rise of at least 5.4 ± 0.63 m, within the narrow timeframe of 9603 ± 288 cal a BP (1σ). The second MWP took place during 8500–8100 cal a BP, adding a total rise of 2.92 ± 0.93 m on the top of background RSL rise, with a two-phase structure where the main phase produced 2.55 ± 0.69 m within a narrow window around 8505 ± 135 cal BP (1σ). Although the rate of RSL rise decreased rapidly to 5.0 mm/a by 7000 cal a BP after ~8100 cal a BP, sea-level data from the WBSC still show an additional rise of 1.45 ± 0.64 m during 7593 ± 78 cal a BP (1σ). These three distinct sea-level jump events, happened before 9500, ~8500, and ~7600 cal a BP, respectively, provide indications of three episodes of enhanced meltwater discharge in the early Holocene, with the latter two closely linked to the decaying history of the Laurentide Ice Sheet.

1. Introduction

During the last deglaciation, global mean sea level (GMSL) rise featured rapid, short-term increases superimposed on a longer-term gradual trend, events commonly referred to as meltwater pulses (MWPs). MWPs studies provide insight into ice sheet melt history and its global impacts, which is vital for improving future sea-level rise predictions. MWPs, initially identified through changes in the growth rate of the reef crest coral *A. palmata* in Barbados, include two significant periods of rapid relative sea-level rise (RSLR), with about 20 m (14–24 m) during MWP-1A (~14100–13600 cal a BP) and 10 m (8–14 m) during MWP-1B (~11400–11100 cal a BP), which are interpreted as the result of massive continental ice melt following catastrophic ice sheet collapse (e.g., Fairbanks, 1989). MWP-1A has been repeatedly confirmed by records from fossil corals (e.g., Bard et al., 1996; Blanchon and Shaw, 1995) and sediment cores (e.g., Hanebuth et al., 2000). However, the existence of MWP-1B remains debated, as the Tahiti barrier reef study found no significant discontinuity in sea-level rise during the MWP-1B period (Bard et al., 2010).

More reports of younger MWPs have further complicated the early Holocene sea-level history. Between ~9800 and 9200 cal a BP, a rapid RSLR of approximately 20 m was identified from paleo-coastal sediments in the western Pacific, which Liu et al. (2004) termed MWP-1C. However, the timing and magnitude of this event are debated due to

* Corresponding author.
E-mail address: tjwangfu@163.com (F. Wang).

https://doi.org/10.1016/j.quascirev.2025.109430
Received 10 February 2025; Received in revised form 15 April 2025; Accepted 18 May 2025
Available online 26 May 2025

widely scattered spatial and temporal data and uncertainty about the melting sources (Smith et al., 2011). Another MWP was triggered by the catastrophic drainage of meltwater from glacial Lake Agassiz-Ojibway in North America associated 8.2 ka cooling event (Barber et al., 1999; Clark et al., 2001; Törnqvist and Hijma, 2012). Törnqvist et al. (2004) were the first to document this event from the near-field Mississippi Delta, identifying two vertically separated peat layers that indicated a total RSLR of 1.19 ± 0.2 m between ~8300 and 8100 cal a BP. This jump has been extensively studied at near-field sites such as the Chesapeake Bay (Cronin et al., 2007), the Mississippi Delta (Li et al., 2012), the Ythan Estuary (YE) in the Scotland (Rush et al., 2023), and the Rhine-Meuse Delta (RMD) in the Netherlands (Hijma and Cohen, 2010, 2019), as well as far-field locations like the Yangtze Delta (Wang et al., 2013). To quantify the magnitude of MWPs, Hijma and Cohen (2010, 2019) separated sea-level rise into a background trend driven by GIA and steady ice melting, and a superimposed jump attributed to rapid meltwater release. Applying this framework, the MWP associated with the 8.2 ka event, was identified occurring~8450–8200 cal a BP, with a total magnitude of 2.11 ± 0.89 m on top of the background RSLR in the RMD region. This jump exhibited a two-phase structure: a primary jump of 1.7 ± 0.6 m at 8440 ± 41 cal a BP, followed by a smaller rise of 0.2 ± 0.2 m at 8220 ± 65 cal a BP (Hijma and Cohen, 2019). The last MWP, documented by Blanchon and Shaw (1995) through analysis of drowned coral elevations and ages in the Caribbean-Atlantic region, was identified as a catastrophic rise event (CRE, equivalent to an MWP) around 7600–7400 cal a BP, involving a 6.5 m rapid RSLR linked to Antarctic Ice Sheet instability. There is ongoing uncertainty regarding the magnitude and sources of the meltwater responsible for this event. Yu et al. (2007) identified a 4.5 m RSLR around 7600 ± 200 cal a BP based on basin studies conducted in crustal rebounding regions of the previously glaciated Swedish Baltic Sea, connecting it to the final collapse of the Labrador sector of the Laurentide Ice Sheet (LIS), a hypothesis supported by Carlson et al. (2008). Bird et al. (2007) suggested a broad inflection phase in RSL of 3–5 m between ~7500 and 7000 cal a BP in Singapore, attributing it to melting of the West Antarctic Ice Sheet. In contrast, Hijma and Cohen (2019) argued that sea-level data from the RMD region only support a smaller, decimeter-scale MWP around 7600–7400 cal a BP.

Far-field sites, distant from former ice sheets, provide critical records of ice-equivalent contributions to RSL change (Pirazzoli, 1991). RSL records from the western Bohai Sea Coast (WBSC), a representative far-field location deep within the Asian continent, offer valuable constrains on the chronology of changes in global grounded ice volume (Bradley et al., 2016). However, since the 1960s, over 100 Holocene sea-level data points (from shelly cheniers, oyster reefs, and sediments) have been generated in the WBSC, recently compiled by Li et al. (2021). These data suggest a rapid RSL rise in the early Holocene, followed by a slowdown ~7500–6800 cal a BP. However, the broad sea-level rise record band compiled from early Holocene data (e.g., Li et al., 2021) has made it challenging to discern detailed history. Many early Holocene sea-level data come from literature cores with imprecise elevations based on estimations or lacking microfossil evidence. Additionally, certain dated materials related to reworked marine shells could lead to age discrepancies. This wide data band obscures precise variations in sea-level changes, complicating efforts to detect finer details. In response, Wang et al. (2020a) developed a high-resolution sea-level index points (SLIPs) dataset using marine-related peaty sediments from WBSC cores, with foraminifera analysis, revealing the local early Holocene RSL rise characterized by a rapid phase of ~8700–7500 cal a BP, followed by a slower increase afterwards. However, the limited availability of early Holocene SLIPs and some local signals within reconstructed RSL have hindered the identification of distinct MWP signals.

In the past two decades, dozens of Holocene cores have been collected by CGS geological projects on the WBSC. After review, 14 cores (Qx01, Qx03, Qx02, Zw15, Tp23, Q7, Qk11, Bt115, Bt117, Ch19, Cz61, Cz65, Cz66, and Cz03) were selected for this study, each containing early Holocene vegetation sediments with ^{14}C dating ages and foraminifera analysis, to generate high-confidence saltmarsh SLIPs. Of these, 9 cores (Qx01, Qx03, Qx02, Zw15, Q7, Cz61, Cz65, Cz66, and Cz03) had previously published SLIPs by Wang et al. (2020a), which have been updated with more ^{14}C dates and foraminifera analysis. The new dataset includes 25 SLIPs spanning the period of ~9800–6900 cal a BP. The altitudes of these SLIPs were revised to account for potential factors such as self-compaction, long-term tectonic subsidence, and the lowering effect of water extraction. This high-resolution early Holocene sea-level record was then used to assess far-field response to MWPs. Combined with near-field datasets, it refines the chronology and magnitude of MWPs and identify potential meltwater sources.

2. Regional setting

Bohai Sea is a semi-enclosed shallow gulf on the innermost portion of East Asia shelf by a 100 km-wide narrow Strait connecting to the northern Yellow Sea (Fig. 1a). The Bohai Sea spans an area of approximately 77,000 km^2, characterized by an average water depth of 18 m. The coastal region, specifically, exhibits depths generally less than 10 m. During the last glacial maximum (LGM), Bohai Sea area was fully exposed and situated about 1000 km away from the coastal line at Asia outer shelf (Qin et al., 1990). Under the context of deglacial GMSL rise, the seawater transgression occurred around the North Yellow Sea to Bohai Strait in the beginning of Holocene (Liu et al., 2004, 2007). Following the early Holocene transgression, the coastline of Bohai Bay retreated generally more than 50–80 km inland around 7000 cal a BP (Xue, 1993; Wang et al., 2015). Subsequently, coastline gradually prograded eastwards mainly caused by Yellow River discharges (e.g., Xue, 1993; Tian et al., 2017). Abundant sediments from Yellow River developed a huge-in-size Holocene coastal system of mud deposit (e.g., Wang et al., 2015, 2020a, 2024).

From a tectonic perspective, the WBSC is located within the Bohai Sea Basin (BSB) (Fig. 1b), the largest Cenozoic rift basin in eastern China. This basin was formed due to mantle dynamics associated with the subduction of the western Pacific plate during the Cenozoic era (Allen et al., 1997). Although the BSB is generally regarded as geologically stable with infrequent seismic activity (Bradley et al., 2016), tectonic subsidence has noticeably accelerated since 12 Ma (Hu et al., 2001; Liu et al., 2016). Liu et al. (2022) quantified the anomalous subsidence in the BSB by removing earlier thermal subsidence and found that Quaternary tectonic subsidence was concentrated in the northwest part of the study area, exceeding 350 m, while other regions remained relatively stable, with vertical deformation between −50 and 150 m (with negative values indicating slight uplift) (Fig. 1c).

Since the 1950s, and especially after the 1970s, extensive groundwater extraction has led to significant land subsidence along the WBSC. Using precise leveling data, Su et al. (2021) documented both the spatial extent and magnitude of this subsidence (Fig. 1c). They reported total subsidence exceeding 0.6 m across the entire WBSC, with declines in deep groundwater exceeding 40 m and shallow groundwater less than 10 m. The most severely affected areas, including the coastal cities of Tianjin, Tanggu, Hangu, and Cangzhou, experienced subsidence of 1.0–2.6 m, corresponding to deep groundwater declines exceeding 70 m.

3. Material and methods

3.1. Cores and sample elevations

The dataset includes 14 cores: 10 onshore cores (Qx01, Qx03, Qx02, Zw15, Tp23, Q7, Cz61, Cz65, Cz66, and Cz03) and 4 offshore cores (Qk11, Bt115, Bt117, and Ch19) (Table 1, Fig. 1c), which together can form three core profiles (P1–P3). P1, perpendicular to the coastline, reveals the early Holocene framework of environmental shifts driven by sea-level change. P2, following the modern coastline, investigates the Holocene initial seawater influences. P3, located inland near the

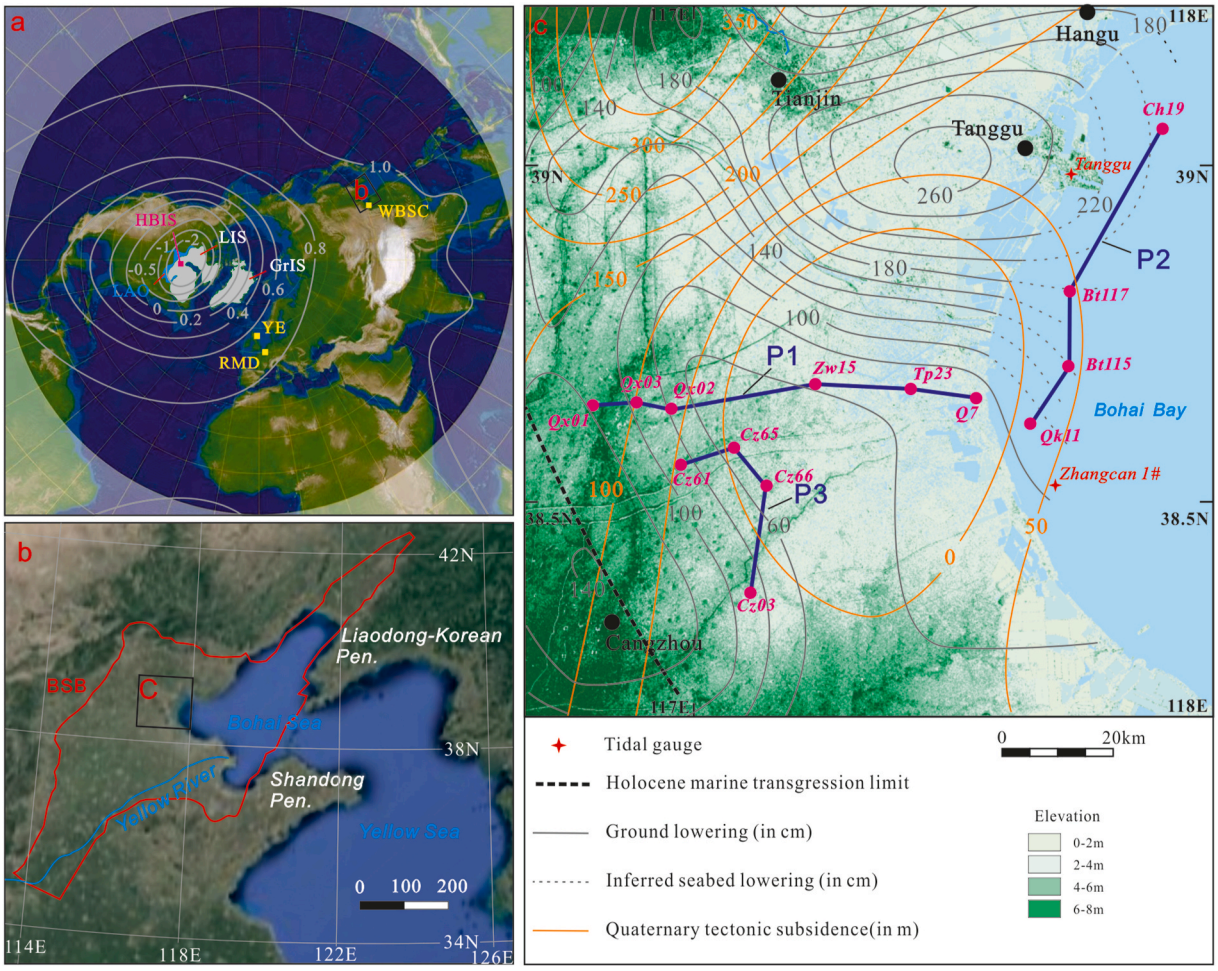

Fig. 1. (a) Overview map of the Northern Hemisphere showing the extent of the Greenland Ice Sheet (GrIS) and Laurentide Ice Sheet (LIS), as well as the position of the Hudson Bay Ice Saddle (HBIS) at ~8800 cal a BP (Dalton et al., 2020) and the Lake Agassiz-Ojibway (LAO) at ~8500 cal a BP (Lajeunesse and St-Onge, 2008). White contours represent the predicted sea-level fingerprint associated with the catastrophic drainage of LAO at ~8400 cal yr BP (cf. Kendall et al., 2008). Key sea-level study sites discussed in the text are highlighted. (b) Map of Northeast Asia showing the geological site of the Cenozoic Bohai Sea Basin (BSB), and the locations of the Western Bohai Sea coast (WBSC); (c) A detailed information of the WBSC with tidal gauges, cores locations, Holocene marine transgression limit (Xue, 1993; Wang et al., 2015), accumulating ground lowering (from Su et al., 2021), and quantified Quaternary tectonic subsidence (from Liu et al., 2022).

Table 1
Cores information for this study.

Core	Position	Elevation/m	Pleistocene base/m	Land subsidence/m (in 1960–2010s)	Quaternary Tectonic deformation	
					Total deformation/m	Average rate/m ka^{-1}
Qx01	N 38°38.9′, E 116°48.9′	5.16	15.4	1.1 ± 0.1	125 ± 25	0.05 ± 0.01
Qx02	N 38°38.9′, E 116°57.4′	3.57	14.8	0.7 ± 0.1	50 ± 25	0.02 ± 0.01
Qx03	N 38°38.9′, E 116°53.7′	4.38	14.1	0.9 ± 0.1	100 ± 25	0.04 ± 0.01
Zw15	N 38°40.4′, E 117°13.3′	1.63	15.2	0.7 ± 0.1	−25 ± 25	−0.01 ± 0.01
Tp23	N 38°40.0′, E 117°24.7′	1.85	17.1	0.7 ± 0.1	−25 ± 25	−0.01 ± 0.01
Q7	N 38°39.4′, E 117°31.5′	3.46	18.9	0.7 ± 0.1	−25 ± 25	−0.01 ± 0.01
Cz61	N 38°33.5′, E 116°58.8′	3.76	14.7	0.8 ± 0.1	50 ± 25	0.02 ± 0.01
Cz65	N 38°34.8′, E 117°04.3′	2.96	13.9	0.6 ± 0.1	0 ± 25	0 ± 0.01
Cz66	N 38°31.5′, E 117°08.0′	3.87	15.0	0.6 ± 0.1	0 ± 25	0 ± 0.01
Cz03	N 38°22.3′, E 117°06.5′	3.94	15.0	0.9 ± 0.1	25 ± 25	0.01 ± 0.01
Ch19	N 39°03.8′, E 117°54.3′	−7.6	17.0	1.9 ± 0.2	75 ± 25	0.03 ± 0.01
Bt117	N 38°48.5′, E 117°42.0′	−4.3	14.1	1.7 ± 0.2	50 ± 25	0.02 ± 0.01
Bt115	N 38°42.0′, E 117°41.9′	−6.0	13.2	1.4 ± 0.2	50 ± 25	0.02 ± 0.01
Qk11	N 38°37.1′, E 117°38.2′	−3.5	14.0	1.0 ± 0.2	25 ± 25	0.01 ± 0.01

Pleistocene base depth values, identified via sedimentary method, can be used as incompressible positions to calculate the compaction loss for samples in strata. Land subsidence value for onshore cores (Qx01, Qx03, Qx02, Zw15, Tp23, Q7, Cz61, Cz65, Cz66, and Cz03) was determined based on cumulative subsidence results from Su et al. (2021), for near shore cores (Qk11, Bt115, Bt117, and Ch19) was estimated based on the trends in cumulative subsidence contour lines for inland regions. The quantified Quaternary tectonic deformation was from Liu et al. (2022), with negative values indicating slight uplift.

Holocene maximum transgression, captures the sensitive late early Holocene environmental changes.

All cores site elevations were tied to the mean sea level (MSL) of National Yellow Sea 85 Datum. The onshore cores were levelled using GPS-RTK system by the CORS network with uncertainty at 2 cm and their rotary drilling error were estimated within 5 cm. The elevations of offshore cores were measured using an echo sounder and corrected in real-time for tidal fluctuations, with a total uncertainty of 10 cm. Rotary drilling errors were estimated to be within 10 cm due to wave-induced challenges. In all cores, logging was conducted with an accuracy of 1 cm, and the sampling thickness was set at 2 cm.

3.2. Radiocarbon dating

A total of 48 samples from early Holocene strata in 14 cores were collected for Accelerator Mass Spectrometry (AMS) ^{14}C dating (Table 2). The analyses were conducted at Beta Analytic Inc. or the School of Archaeology and Museology, Peking University. The dated materials included 43 extracted plant fragments, one terrestrial gastropod, and four bulk organic sediments. All conventional radiocarbon dates were calibrated individually to calendar years relative to 1950 CE using OxCal 4.4 (Bronk Ramsey, 2009) with the IntCal20 calibration curve (Reimer et al., 2020), yielding 'unmodelled' ages (Table 2). For saltmarsh SLIPs within the age-depth series, Bayesian models were applied to refine the calibrated age ranges, resulting in 'modelled' ages. Three separate Sequence () models were constructed for inland sites (Qx01, Qx03, Qx02, Cz61, Cz65, Cz66, and Cz03), coastal sites (Zw15, Tp23, and Q7), and offshore sites (Qk11, Bt115, Bt117, and Ch19).

3.3. Sedimentary identifications and sea-level indicative meanings

Sediment cores were photographed and logged in details including Munsell color, composition, physical sedimentary structure, organics, macrofossils, and bioturbations. To help to determine the sedimentary environments, samples in potential Holocene marine-related sections were taken to identify foraminifera. Picked out from the >63 μm fraction of sediment under microscope, the foraminifera analysis involved basic abundance (number of individuals per gram), some with assemblage characteristics. All SLIPs in this study are high confidence high marsh vegetation samples with ^{14}C ages.

Table 2
AMS^{14}C ages from early Holocene sediments on WBSC.

Sample ID	depth/m	Dated materials	δ^{13}C	Measured^{14}C age/a BP	Conventional ^{14}C age/a BP	Unmodelled calibrated age (cal a BP)		Lab. No.
						1 σ	2σ	
Qx01-1	9.16	plant fragment	−27.4	6220 ± 40	6220 ± 40	7021–7240	6995–7254	329636
Qx01-2	11.39	plant fragment	−25.3	7010 ± 30	7010 ± 30	7794–7925	7752–7934	329640
Qx01-3	13.05	plant fragment	−25.1	7200 ± 30	7200 ± 30	7975–8020	7938–8159	329646
Qx03-1	8.63	plant fragment	−26.7	6440 ± 40	6410 ± 40	7275–7420	7263–7420	353798
Qx03-2	9.60	plant fragment	−28.2	6740 ± 40	6690 ± 40	7510–7606	7475–7659	353800
Qx03-3	12.40	plant fragment	−28.3	7330 ± 40	7280 ± 40	8025–8167	8014–8178	353802
Qx02-1	7.27	plant fragment	−25.7	6360 ± 30	6350 ± 30	7180–7314	7167–7414	333329
Qx02-2	8.98	plant fragment	−26.3	6620 ± 30	6600 ± 30	7433–7560	7429–7566	333330
Qx02-3	10.97	plant fragment	−27.2	7060 ± 30	7020 ± 30	7797–7927	7782–7936	333331
Qx02-4	11.9	plant fragment	−26.6	7180 ± 40	7150 ± 40	7940–8007	7870–8025	333332
Qx02-5	12.42	plant fragment	−26.3	7160 ± 40	7140 ± 40	7936–8007	7869–8021	333333
Zw15-1	12.60	plant fragment	−25.0	7450 ± 40	7450 ± 40	8202–8330	8184–8357	356208
Zw15-2	13.50	plant fragment	−25.5	7650 ± 40	7640 ± 40	8384–8453	8375–8536	356209
Zw15-3	14.17	plant fragment	−26.5	7740 ± 40	7720 ± 40	8448–8542	8417–8589	356211
Zw15-4	15.05	plant fragment	−25.8	7700 ± 40	7690 ± 40	8419–8519	8400–8586	356210
Tp23-1	14.10	plant fragment	NA	NA	7610 ± 40	8375–8423	8345–8519	BA091542
Tp23-2	16.70	plant fragment	NA	NA	8035 ± 45	8780–9013	8654–9078	BA091544
Tp23-3	16.80	plant fragment	NA	NA	8915 ± 45	9916–10179	9827–10204	BA091545
Tp23-4	17.00	plant fragment	NA	NA	9380 ± 55	10515–10684	10425–10755	BA091546
Q7-1	17.20	plant fragment	−28.0	8040 ± 40	7990 ± 40	8777–8991	8650–9000	357153
Q7-2	18.85	organic sediment	−24.6	9130 ± 40	9140 ± 40	10235–10368	10225–10485	357157
Qk11-1	11.00	plant fragment	−27.8	7900 ± 30	7850 ± 30	8590–8690	8546–8765	467243
Qk11-2	11.40	plant fragment	−27.3	8030 ± 30	7990 ± 30	8778–8990	8655–8998	467242
Qk11-3	11.70	plant fragment	−27.3	8040 ± 30	8000 ± 30	8779–8993	8724–9002	467241
Qk11-4	11.80	plant fragment	−27.3	8120 ± 30	8080 ± 30	8990–9077	8784–9124	467240
Qk11-5	13.40	plant fragment	−26.7	8390 ± 30	8360 ± 30	9315–9454	9293–9470	467244
Qk11-6	13.95	plant fragment	−24.9	8430 ± 30	8430 ± 30	9435–9488	9328–9530	467245
Bt115-1	11.10	plant fragment	NA	NA	8190 ± 40	9027–9260	9019–9276	BA091538
Bt117-1	11.28	Plant fragment	−28.8	7910 ± 30	7850 ± 30	8590–8690	8546–8765	426149
Bt117-2	13.95	organic sediment	−24.3	9110 ± 30	9120 ± 30	10230–10288	10216–10378	426150
Ch19-1	15.95	plant fragment	NA	NA	8765 ± 40	9685–9891	9555–10106	BA06817
Ch19-2	16.65	freshwater gastropod	NA	NA	9760 ± 55	11161–11244	10878–11269	BA06818
Cz61-1	6.20	organic sediment	−23.9	6080 ± 30	6100 ± 30	6901–7149	6856–7157	406824
Cz61-2	9.73	plant fragment	−19.6	6670 ± 30	6760 ± 30	7580–7658	7574–7669	403397
Cz61-3	11.04	plant fragment	−27.5	7040 ± 30	7000 ± 30	7792–7921	7742–7932	403398
Cz61-4	12.90	plant fragment	−28.0	7210 ± 30	7160 ± 30	7959–8010	7934–8022	403399
Cz65-1	9.58	plant fragment	−27.2	7040 ± 30	7000 ± 30	7792–7921	7742–7932	399708
Cz65-2	11.50	plant fragment	−27.1	7280 ± 30	7250 ± 30	8012–8165	7980–8170	399709
Cz65-3	12.60	organic sediment	−23.0	7590 ± 30	7620 ± 30	8385–8420	8368–8514	399710
Cz66-1	8.14	plant fragment	−27.4	6750 ± 30	6710 ± 30	7518–7605	7510–7660	339714
Cz66-2	10.03	plant fragment	−26.6	6820 ± 30	6790 ± 30	7610–7667	7582–7676	399715
Cz66-3	12.49	plant fragment	−21.7	7250 ± 30	7220 ± 30	7972–8034	7960–8168	399716
Cz66-4	13.63	plant fragment	−27.6	7710 ± 30	7670 ± 30	8407–8518	8400–8540	399718
Cz03-1	7.51	plant fragment	−26.7	6260 ± 30	6230 ± 30	7027–7245	7010–7253	395029
Cz03-2	9.22	plant fragment	−27.3	6680 ± 30	6640 ± 30	7488–7570	7432–7576	395030
Cz03-3	9.34	plant fragment	−20.0	6580 ± 30	6660 ± 30	7507–7575	7434–7583	395031
Cz03-4	10.23	plant fragment	−27.2	6940 ± 30	6900 ± 30	7680–7751	7670–7825	395032
Cz03-5	12.4	plant fragment	−27.2	7330 ± 30	7290 ± 30	8031–8168	8025–8173	395034

The indicative meanings of salt marshes were defined following Chapter 34 of the *Handbook of Sea-Level Research*, which specifies that high marshes form in the tidal range between the highest astronomical tide (HAT) and mean high water (MHW) (Hijma et al., 2015).

3.4. Tidal datums

To determine the indicative meaning and range of each SLIP collected from this region, 41 years (1950.1–1990.12) of tidal observations from two local tide gauges (Tanggu and Zhangcan 1#) (DPA and NMDC, 1991) were analyzed. Tidal levels, including highest astronomical tide (HAT), mean lower low water (MLLW), mean higher high water (MHHW), mean low water (MLW), MHW, mean tidal level (MTL), LAT, are broadly consistent in two gauges (Table 3).

SLIPs are generally defined relative to tidal levels, but the heights of these datums have fluctuated throughout the Holocene due to changes in sea level and shifts in coastal configuration and water depth (Hijma and Cohen, 2019). Although paleo-tidal studies suggest stronger tidal currents occurred during the early Holocene in the eastern Bohai Sea region (Chen and Zhu, 2012; Yao et al., 2017), likely influenced by a semi-enclosed bay system that extended from the East China Sea and the Yellow Sea into the Bohai Sea (Uehara and Saito, 2003; Chen and Zhu, 2012). The possibility of increased tidal amplitude during this period remains highly uncertain. Given that the Bohai Sea has an average depth of only 18 m currently, in the early Holocene when sea levels were much lower than today, its tidal waves would have faced even greater frictional dissipation in these shallow coastal waters. For example, Wang et al. (2020b) simulated that the mean spring high water (MSHW) along the open coast of the East China Sea in the early Holocene (~7.6 ka BP) ranged from 1.6 to 1.8 m, about 70 % of its modern value (cf. Wang et al., 2013). Due to the lack of quantitative data on these changes, this study assumes constant modern tidal levels based on tide gauges near the sampling sites. Moreover, as tidal amplitude remains stable over short timescales, its deviations introduce only a systematic bias, making their impact on MWP magnitude estimates negligible.

Tidal levels from the Zhangcan 1# gauge and the Tanggu gauge (Table 3) were applied to the southern (core sites Qx01, Qx03, Qx02, Zw15, Tp23, Q7, Cz61, Cz65, Cz66, Cz03, Qk11, Bt115, and Bt117) and northern (core site of Ch19) parts of the WBSC area, respectively.

3.5. Correction of tectonic effects, water extraction effects, and sediment compaction effects

Using Quaternary vertical deformation values for each location (−25 to 125 m, with an uncertainty of 25 m) (Liu et al., 2022) (Table 1, Fig. 1c), divided by 2.58 Ma, we calculated the average tectonic deformation rates for each core site to adjust the SLIPs.

Since the 1950s, extensive groundwater extraction, primarily from deep aquifers, has caused significant land subsidence along the WBSC, with cumulative subsidence ranging from 0.6 to 2.6 m (Su et al., 2021). As the offshore drilling sites are only a few kilometers from the coastline, we infer that deep groundwater extraction has similarly contributed to land subsidence in these areas. Based on the trends in cumulative subsidence contour lines for onshore regions, we estimated and supplemented the subsidence for the offshore sites (Fig. 1c). The elevation of each sample site was adjusted by adding the cumulative subsidence, which ranges from 0.6 to 1.9 m depending on the location (Table 1). For onshore areas, an uncertainty of 0.1 m was applied, corresponding to half the contour interval in the land subsidence distribution map. For offshore areas, this uncertainty was increased to 0.2 m to account for additional variability.

In the WBSC Holocene sequence, due to sufficient local sediment supply, thick peats are absent, with basal and intercalated peaty layers typically being centimeter-thick and containing organic matter contents of 1–4 %, while Holocene marine deposits mainly consist of unconsolidated mud with organic matter contents of 0.5–1.0 % (e.g., Wang et al., 2015). This study follows the suggestions of Xiong et al. (2018) to correct for post-depositional compaction in SLIPs. The coastal sediments experience increasing compaction over time, with the total lowering of SLIPs estimated at 10 % of the initial thickness of the compressible sequence(s) beneath the dated position, scaled proportionally to the post-depositional lapse time over the past 9000 years (Xiong et al., 2018).

3.6. Sea-level trends analyses

As described above, SLIPs can be further corrected for elevations by accounting for all lowering effects due to water extraction, tectonic deformation, and coastal strata self-compaction. The vertical uncertainty is calculated by taking the square root of the quadratic sum of all individual sources of uncertainty (e.g., Hijma et al., 2015). An integrated Gaussian process EIV-IGP model of Cahill et al. (2015, 2016) was employed to estimate the non-linear trend underlying the noisy sea-level data and to generate a sea-level curve with 1σ and 2σ probabilistic intervals. For the calculation of MWP magnitudes, we follow the approach outlined in Hijma and Cohen (2019) and apply the formula provided in the HOLSEA data repository (Hijma and Cohen, 2019).

4. Results and interpretation

4.1. The early Holocene sedimentary facies identification and SLIPs

The early Holocene archives in all 14 cores was underlain by dark greenish to light greyish stiff mud (Pleistocene basement). The stiff mud is characterized by iron–oxides, calcareous nodules, and leaching structures, generally demonstrating paleosol features from subaerial exposure. No foraminifera or marine mollusk remains were identified in this unit. We interpreted these Pleistocene basement deposits underwent a context of floodplain with prolonged drought conditions during the LGM. The Pleistocene basement stiff mud decreases eastward along profile P1, from −9.0 m in inland core Qx01 to −15.4 m in coastal core Q7, decreases northward along offshore profile P2, from −17.5 m in core Qk11 to −24.6 m in core Ch19, and remains relatively stable around −10 m in elevation along inland profile P3 (Table 1; Fig. 2). Above the Pleistocene basement, the early Holocene archives reveal a transgressive sequence. The Holocene stratigraphic framework and the sedimentary facies identification are provided as follows.

4.1.1. Section of basal freshwater marsh

In five cores from modern coastal areas, Ch19, Bt117, Bt115, Q7, and Tp23, stiff mud was generally covered by a layer of basal peat with few decimeters thick (Fig. 2). No foraminifera or marine shells were found, instead a rich diversity of freshwater mollusk was present, such as at the depth of 16.64–16.70m from core Ch19, where over 103 individuals from six species were found in approximately 50g of peat. These included *Gyraulus albus* (55 individuals), *Hippeutis cantori* (28), *Planorbarius corneus* (10), *Parafossarulus striafulus* (6), *Pseudophysa grabaui* (6), and *Succinen hopeensis* (1). We interpreted these peats as having

Table 3
Reference tidal levels (DPA and NMDC, 1991) for study area (m, elevation, MSL).

Gauge	Location	HAT	MHHW	MHW	MTL	MLW	MLLW	LAT
Tanggu	N 38°59.0′, E 117°47.0′	1.98	1.29	1.15	−0.02	−1.29	−1.71	−2.52
Zhangcan 1#	N 38°32.3′, E 117°40.0′	1.98	1.31	1.18	−0.02	−1.29	−1.71	−2.62

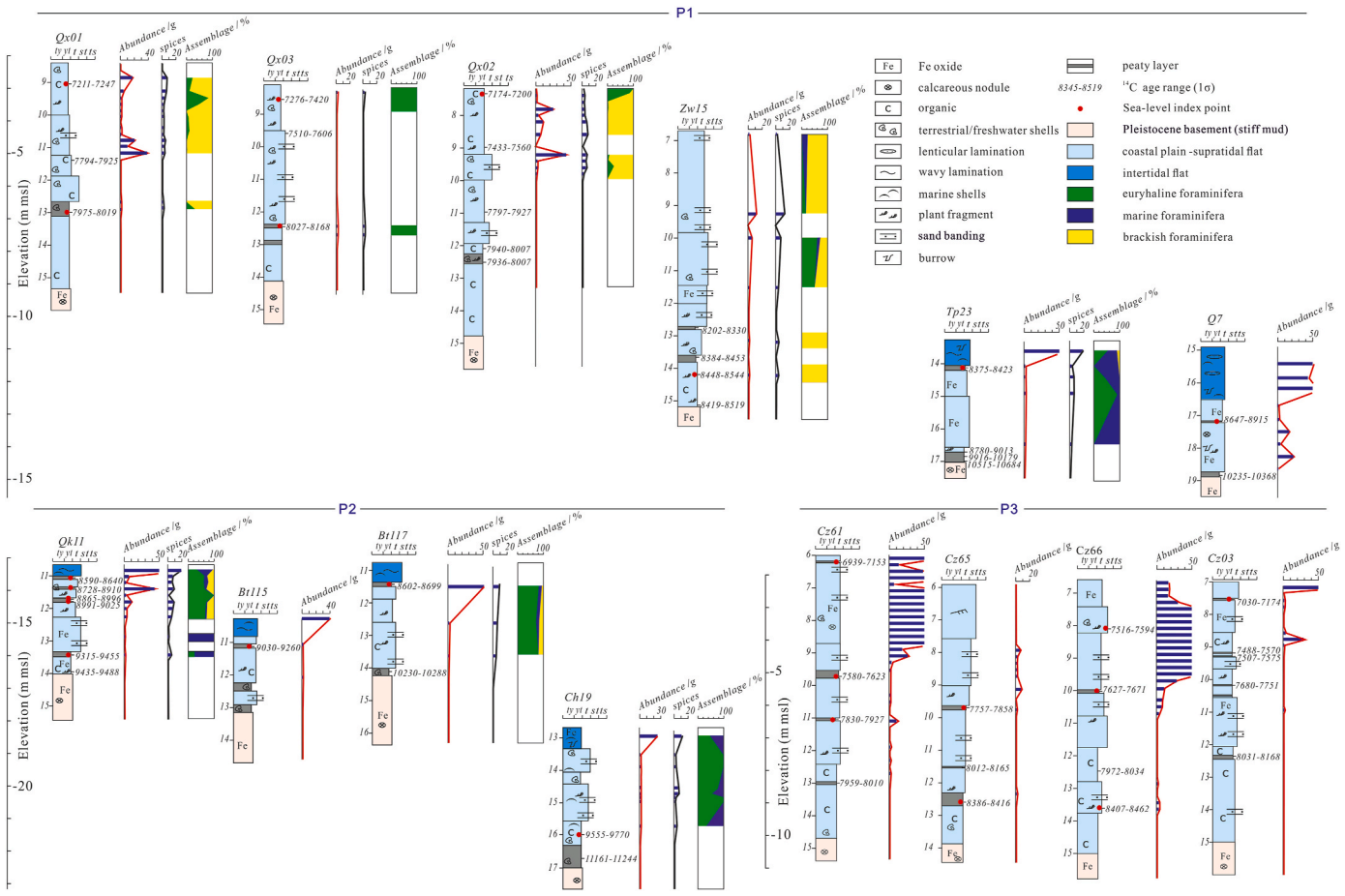

Fig. 2. Three sedimentological profiles (P1, P2, and P3) along the WBSC, illustrating Early Holocene marine-related sequences with foraminiferal analysis and 1σ age ranges (for SLIPs with modelled ages). Foraminifera analysis includes basic abundance, with some incorporating assemblage characteristics. Foraminifera abundance values > 50/g are displayed as 50/g for clarity.

developed in a long-term freshwater marsh environment during the early Holocene, under a regional warm and humid climate, before being eventually inundated by marine flooding.

In the remaining cores, the basal sediments, commonly muds with low organic content, were hard to distinguish from the overlying strata. As a result, we combined these sediments into a single section in the subsequent analysis.

4.1.2. Section of coastal plain–supratidal flat

In all 14 cores, above the basal peat or stiff mud, early Holocene sediments were made of soft yellowish grey mud and sand, with vegetation fragments dispersed and localized enrichment in thin peaty mud (Fig. 2). Within these sediments freshwater mollusks were frequently preserved, including *Gyraulus albus*, *Bithynia fuchsiana*, *Lamprotula tientsinensis*, *Bellamya purificata*, *Alocinma longicornis*, *Gyraulus convexiusculus*, *Hippeutis cantori*, *Polypylis hemisphaerula*, and *Pseudophysa grabaui*, along with opercula. While marine mollusks were rarely observed.

Generally, foraminifera in this section were sporadically and sparsely present, with euryhaline, marine or brackish species dominating depending on locations. For horizons rich in foraminifera, abundance can up to 10–200/g, however, assemblage analysis in cores Qx01, Qx03, Qx02, Zw15, Qk11 shows these high abundance foraminifera were primarily dominated by brackish and euryhaline species (Fig. 2), such as *Nonion glabrum*, *Nonionella auricula*, *Ammonia beccarii* vars. We interpret that these sediments were formed under contexts of infrequent extreme tides or weather events, or brackish condition. Depths containing foraminifera are interpreted as representing supratidal flats, while those lacking foraminifera are interpreted as coastal plains with minimal or unclear marine influence.

4.1.3. Section of intertidal flat

In coastal regions such as core sites Qk11, Bt115, Bt117, Ch19, and Q7, a meter-scale layer of grayish sand and silt, characterized by wavy-lenticular and flaser bedding with few muddy interlayers, caps the entire early Holocene transgressive sequence (Fig. 2). Marine mollusks and traces of bioturbation are commonly found in this section. Marine mollusk identification shows they contain subtidal spices such as *Ruditapes philippinarum*, *Crassostrea gigas*, *Potanocorbula laevis*, and tidal spices such as *Meropesta sinojaponica*, *Rissoina bureri*, and *Mitrella bella.* Foraminifera in this section are present abundantly (20–300/g), consisting of various euryhaline and marine species.

We interpret these sediments as having been deposited under conditions of regular tidal submersion, as intertidal flat environments.

4.2. Early Holocene saltmarsh SLIPs

The diverse coastal vegetation is capable of tolerating a wide range of environments, from freshwater zones to intertidal zones near mean sea level (e.g., Shennan et al., 1995). Within the WBSC region, 25 dated vegetation samples were found to preserve foraminifera. Samples with sparse foraminifera included various euryhaline, marine, or brackish species. In samples where foraminifera were more abundant, brackish and euryhaline species dominated (Fig. 2). These assemblages closely resemble those in modern supratidal and high marsh environments along East China coasts, where foraminifera are typically dominated by

brackish and euryhaline taxa but range in abundance (e.g., Wang et al., 2013; Li et al., 2010, 2016). Furthermore, the common occurrence of freshwater mollusks and thin-shelled fragments, coupled with the rarity of marine mollusks, suggests that the sampled vegetation thrived in a land–sea transitional environment. Of these 25 samples, 22 were found within coastal plain–supratidal flat deposits with conformable contacts. The remaining 3 samples (Qk11-1, Bt117-1, and Tp23-1) were conformably above supratidal flat deposits but unconformably overlain by tidal flat sediments (details in Appendix data), indicating an abrupt transition from supratidal to intertidal conditions. These stratigraphic contexts indicate these vegetation samples having formed under high marsh conditions prior to subsequent marine inundation, and thus justifies their classification as high marsh SLIPs.

Among these SLIPs, 11 were derived from previously published cores by Wang et al. (2020a), including IDs: Qx01-1, Qx01-3, Qx03-1, Qx02-1, Q7-1, Cz61-1, Cz61-2, Cz65-1, Cz66-1, Cz66-2, and Cz03-1. Five SLIPs (IDs: Qx03-3, Zw15-3, Cz61-3, Cz65-3, and Cz66-4) were identified by updating cores from the same study with additional radiocarbon dates and foraminiferal analyses. The remaining nine SLIPs were newly established in this study, including one from an inland core (Tp23-1) and eight from offshore cores (Qk11, Bt115, Bt117, and CH19), with IDs: Tp23-1, Qk11-1, Qk11-2, Qk11-3, Qk11-4, Qk11-5, Bt115-1, Bt117-1, and CH19-1.

These SLIPs can be further corrected for lowering, taking into account all lowering effects by water extraction, tectonic deformation and coastal strata self-compaction. To contribute to the global standardized SLIPs database, we followed the guidance of the database template and detailed instructions of Khan et al. (2019). For each SLIP, evidence for sample type, correction for post-depositional lowering, and the indicative meanings are compiled in Table 4.

4.3. Early Holocene relative sea-level changes

The 25 SLIPs along the WBSC are shown in Fig. 3, with paleo-RSL versus the modelled calibrated ages (2 σ). All data fit well with each other, demonstrating a smoothly and concentrated early Holocene RSL curve between c. 9800 and 6900 cal a BP. Using the 1 σ modelled calibrated ages, we further plotted 1 σ and 2 σ confidence intervals of the EIV-IGP model of Cahill et al. (2015, 2016). During this approximately 2900-year period, the reconstructed RSL changes using the EIV-IGP model indicate that the rate of RSL rise was relatively high before 8000 cal a BP, around 7–8 mm/a. After 8000 cal a BP, the rate rapidly decreased to 5.0 mm/a by 7000 cal a BP (Fig. 3). Considering that the EIV-IPG model employs a covariance function that imposes smoothness, the sea-level jump signal may not be fully captured in the EIV-IPG modeling. Therefore, it should be followed by a comparison of the results. Specifically, the rate of early-Holocene RSL rise varied significantly before 9500, ~8500, and ~7600 cal a BP, marking three distinct phases of MWPs (Fig. 3).

5. Discussion

5.1. MWP before 9500 cal a BP

As previously noted, after the onset of the Holocene, typical fresh basal peats developed at modern coastal sites under a prolonged warm and humid climate. However, in offshore core Ch19 (modern elevation: −7.6 m), ~70 cm of basal peat transitioned into supratidal deposits, where the earliest high marsh SLIP in the study area, Ch19-1, was identified, dated to 9555–9770 cal a BP (1σ) (Fig. 2). Nearly simultaneously, in the shallower-water core Qk11 (modern elevation: −3.5 m), the previously exposed Pleistocene basement was transformed into a coastal plain and then into a supratidal flat, in response to this drowning. A plant sample (Qk11-6) collected from the coastal plain directly above the Pleistocene basement yielded an age of 9435–9488 cal a BP (1σ), which was shortly followed by the establishment of a high marsh environment, dated after 9315–9455 cal a BP (1σ) by sample Qk11-5 (Fig. 2). These nearly coeval transitions across different original geomorphic settings suggest a possible rapid sea-level rise event during this period.

When the relative elevations of early Holocene SLIPs are examined (Figs. 3 and 4), this sea-level jump becomes more evident. SLIPs from ~9500 to 8600 cal a BP follow a consistent trend, indicating a relatively steady RSLR from about −17.4 to −15.0 m MSL In contrast, the SLIP Ch19-1, with a 1σ age of 9684–9891 cal a BP and an elevation of −22.81 m MSL, significantly deviates from this trend, pointing to a rapid RSL rise before 9500 cal a BP. Due to the limited number of SLIPs, it is insufficient to precisely determine the onset time or amplitude of this jump; however, its end time must precede 9315–9454 cal a BP (1σ) and at least an RSLR of 5.4 ± 0.63 m occurred within the narrow timeframe of 9603 ± 288 cal a BP (1σ). This rapid sea-level rise triggered the Holocene inundation of the WBSC, depositing transgressive supratidal sediments across the modern offshore region, as recorded at core sites Ch19, Qk11, Bt115, and Bt117.

In other Asian regions, paleo-coastal sediment records from this period are similarly typically located in offshore areas (e.g., Liu et al., 2004; Wang et al., 2010; Xiong et al., 2018; Tjallingii et al., 2010). However, the limited availability of samples and the challenges in accurately identifying SLIPs have hindered the precise recognition of this event. Nevertheless, a rapid sea-level rise during a similar timeframe has been documented in the PRD region (Xiong et al., 2018), characterized by a sharp rise around this period followed by a notable deceleration. While the exact timing and magnitude remain poorly constrained, evidence from these far-field Asian sites supports the occurrence of a meltwater pulse before 9500 cal a BP.

The mechanisms behind this rapid sea-level rise are likely complex, involving multiple global ice sheets, with many uncertainties remaining regarding their contributions under a climatic worming setting. The North American LIS showed an accelerated retreat along the southwestern to western margin and over Hudson Bay, accompanied by a 0.4–0.6 ‰ decrease in Labrador Sea planktonic $\delta^{18}O$ roughly between 11 and 9 ka BP (Carlson et al., 2008). Meanwhile, the Scandinavian Ice Sheet (SIS) entered its final stages of decay after 9.7 ka BP, although its specific meltwater contribution remains uncertain (e.g., Stroeven et al., 2016). In the Southern Hemisphere, recent studies of the Antarctic Ice Sheet (AIS) (Spector et al., 2017; Nichols et al., 2019; Jones et al., 2022) suggest that while its meltwater contribution during the early Holocene was relatively modest compared to the LIS, it was still significant. Jones et al. (2022) modelled AIS ice volume changes and identified a period of accelerated melting between 10 and 9.5 ka BP, contributing approximately 800 Gt/a, equivalent to a global sea-level rise of about 2.4 mm/a, primarily from the Ross Sea and Weddell Sea sectors.

5.2. MWP associated with 8.2 ka cooling event

Sedimentary records during ~8500–8100 cal a BP show several-meters-thick supratidal deposits in offshore areas, such as Qk11, Bt117, and Q7, which were eventually submerged, while the newly formed supratidal zone extended 40–60 km inland to sites including Qx03, Cz65, and Cz66 (Fig. 2). In the offshore region, such as at sites Qk11 and Bt117, two dates (IDs: Qk11-1 and Bt117-1) obtained from peaty layers, just beneath a regionally traceable tidal submergence contact, yielded ages of 8590–8640 and 8602–8699 cal a BP (1σ), respectively. The combined age of 8602–8640 cal a BP suggests a maximum onset around 8.6 ka. This abrupt submergence also transformed the former Pleistocene basement in more inland areas, such as site Zw15, into coastal plain and then supratidal flat. A dated plant sample from supratidal flat sediments at this site yielded an age of 8448–8544 cal a BP (1σ), indicating a minimum onset of the MWP at around 8.5 ka. We used the earliest SLIP Qk11-1, 8590–8640 cal a BP (1σ), within this initial age range to calculate the magnitude of the sea-level jump, and tentatively assigned the endpoint to 8025–8167 cal a BP

Table 4
Saltmarsh SLIPs from the WBSC.

ID	OxCal (2σ) unmodelled age/cal a BP	OxCal (1σ) modelled age/cal a BP	OxCal (2σ) modelled age/cal a BP	Depth /m	Depth to consolidated substrate /m	Sample elevation & error /m, MSL	sample type	Supporting evidence			Indicative meaning	Indicative meaning /m, MSL	RSL & range /m	Post-depositional correction for sample elevation			Corrected RSL & range/m
								Foraminifera		Macrofossil remains				Compaction/ m	Tectonic deformation & error/m	Ground lowering & error/ m	
								Abun. /g	Assemb.								
Qx01-1	6995–7254	7211–7247	7188–7263	9.16	6.2	−4.00 ± 0.05	highmarsh	4	Ng		HAT – MHW	1.58 ± 0.40	−5.58 ± 0.40	0.53	0.36 ± 0.07	1.2 ± 0.1	−3.49 ± 0.42
Qx01-3	7938–8159	7975–8019	7943–8035	13.05	2.4	−7.89 ± 0.05	highmarsh	<1	Ab, Cs	thin-shelled fragments	HAT – MHW	1.58 ± 0.40	−9.47 ± 0.40	0.23	0.40 ± 0.08	1.2 ± 0.1	−7.64 ± 0.42
Qx03-1	7263–7424	7276–7420	7267–7422	8.63	5.5	−4.25 ± 0.05	highmarsh	<1	Ab Em,	thin-shelled fragments	HAT – MHW	1.58 ± 0.40	−5.83 ± 0.40	0.49	0.29 ± 0.07	1.0 ± 0.1	−4.05 ± 0.42
Qx03-3	8014–8178	8027–8168	8019–8175	12.40	1.7	−8.02 ± 0.05	highmarsh	<1	Ab Em,	*Bithynia fuchsiana*	HAT – MHW	1.58 ± 0.40	−9.60 ± 0.40	0.17	0.32 ± 0.08	1.0 ± 0.1	−8.11 ± 0.42
Qx02-1	7167–7414	7174–7200	7164–7255	7.27	7.5	−3.70 ± 0.05	highmarsh	<1	Ab	thin-shelled fragments	HAT – MHW	1.58 ± 0.40	−5.28 ± 0.40	0.66	0.22 ± 0.07	0.8 ± 0.1	−3.60 ± 0.42
Zw15-3	8417–8589	8448–8544	8421–8589	14.17	1.0	−12.54 ± 0.05	highmarsh	<1	Ab		HAT – MHW	1.58 ± 0.40	−14.12 ± 0.40	0.11	−0.08 ± 0.08	0.6 ± 0.1	−13.49 ± 0.42
Tp23-1	8345–8519	8375–8423	8349–8517	14.10	3.0	−12.25 ± 0.05	highmarsh	<1	En, Pt	thin-shelled fragments	HAT – MHW	1.58 ± 0.40	−13.83 ± 0.40	0.31	−0.08 ± 0.08	0.7 ± 0.1	−12.90 ± 0.42
Q7-1	8650–9000	8647–8915	8644–8993	17.20	1.7	−13.74 ± 0.05	highmarsh	3	N/A		HAT – MHW	1.58 ± 0.40	−15.32 ± 0.40	0.19	−0.09 ± 0.09	0.7 ± 0.1	−14.52 ± 0.43
Cz61-1	6856–7157	6939–7153	6890–7158	6.20	8.5	−2.44 ± 0.05	highmarsh	<1	N/A		HAT – MHW	1.58 ± 0.40	−4.02 ± 0.40	0.71	0.21 ± 0.07	0.9 ± 0.1	−2.20 ± 0.42
Cz61-2	7574–7669	7580–7623	7575–7656	9.73	5.0	−5.97 ± 0.05	highmarsh	<1	N/A		HAT – MHW	1.58 ± 0.40	−7.55 ± 0.40	0.46	0.23 ± 0.08	0.9 ± 0.1	−5.96 ± 0.42
Cz61-3	7742–7932	7830–7927	7790–7934	11.04	3.7	−7.28 ± 0.05	highmarsh	12	N/A		HAT – MHW	1.58 ± 0.40	−8.86 ± 0.40	0.35	0.24 ± 0.08	0.9 ± 0.1	−7.37 ± 0.42
Cz65-1	7742–7932	7757–7858	7723–7917	9.58	4.3	−6.62 ± 0.05	highmarsh	<1	N/A		HAT – MHW	1.58 ± 0.40	−8.20 ± 0.40	0.41	−0.08 ± 0.08	0.6 ± 0.1	−7.37 ± 0.42
Cz65-3	8368–8514	8386–8416	8370–8441	12.6	1.3	−9.64 ± 0.05	highmarsh	<1	N/A		HAT – MHW	1.58 ± 0.40	−11.22 ± 0.40	0.13	−0.08 ± 0.08	0.6 ± 0.1	−10.67 ± 0.42
Cz66-1	7510–7660	7516–7594	7509–7614	8.14	6.9	−4.27 ± 0.05	highmarsh	367	N/A	thin-shelled fragments	HAT – MHW	1.58 ± 0.40	−5.85 ± 0.40	0.63	−0.08 ± 0.08	0.6 ± 0.1	−4.80 ± 0.42
Cz66-2	7582–7676	7627–7671	7599–7682	10.03	5.0	−6.16 ± 0.05	highmarsh	11	N/A		HAT – MHW	1.58 ± 0.40	−7.74 ± 0.40	0.46	−0.08 ± 0.08	0.6 ± 0.1	−6.86 ± 0.42
Cz66-4	8400–8540	8407–8462	8398–8523	13.63	1.4	−9.76 ± 0.05	highmarsh	3	N/A		HAT – MHW	1.58 ± 0.40	−11.34 ± 0.40	0.14	−0.08 ± 0.08	0.6 ± 0.1	−10.68 ± 0.42
Cz03-1	7010–7253	7030–7174	7007–7202	7.51	7.5	−3.57 ± 0.05	highmarsh	2	N/A	thin-shelled fragments	HAT – MHW	1.58 ± 0.40	−5.15 ± 0.40	0.64	0.07 ± 0.07	0.9 ± 0.1	−3.54 ± 0.42
Qk11-1	8546–8765	8590–8640	8546–8697	11.00	3.0	−14.50 ± 0.12	highmarsh	7	Ab, Na		HAT – MHW	1.58 ± 0.40	−16.08 ± 0.42	0.32	0.09 ± 0.09	0.9 ± 0.2	−14.77 ± 0.47
Qk11-2	8655–8998	8728–8910	8653–8963	11.40	2.6	−14.90 ± 0.12	highmarsh	44	Ab, Na, Ag	*Bithynia fuchsiana*	HAT – MHW	1.58 ± 0.40	−16.48 ± 0.42	0.28	0.09 ± 0.09	0.9 ± 0.2	−15.21 ± 0.47
Qk11-3	8724–9002	8865–8996	8787–9001	11.70	2.3	−15.20 ± 0.12	highmarsh	10	Ab, Na, Ag		HAT – MHW	1.58 ± 0.40	−16.78 ± 0.42	0.25	0.09 ± 0.09	0.9 ± 0.2	−15.54 ± 0.47
Qk11-4	8784–9124	8991–9025	8902–9120	11.80	2.2	−15.30 ± 0.12	highmarsh	10	Ab, Na, Ag		HAT – MHW	1.58 ± 0.40	−16.88 ± 0.42	0.24	0.09 ± 0.09	0.9 ± 0.2	−15.65 ± 0.47
Qk11-5	9293–9470	9315–9455	9293–9470	13.40	0.6	−16.90 ± 0.12	highmarsh	<1	Ab	*Bithynia fuchsiana*	HAT – MHW	1.58 ± 0.40	−18.48 ± 0.42	0.07	0.09 ± 0.09	0.9 ± 0.2	−17.42 ± 0.47
Bt115-1	9019–9276	9030–9260	9022–9275	11.10	2.1	−17.10 ± 0.12	highmarsh	~1	N/A	leafs	HAT – MHW	1.58 ± 0.40	−18.68 ± 0.42	0.23	0.18 ± 0.09	1.4 ± 0.2	−16.87 ± 0.47
Bt117-1	8546–8765	8602–8699	8593–8767	11.35	2.8	−15.85 ± 0.12	lowmarsh	83	Ab, Em		HAT – MHW	1.58 ± 0.40	−17.26 ± 0.42	0.29	0.17 ± 0.09	1.8 ± 0.2	−14.99 ± 0.47
Ch19-1	9555–10106	9555–9770	9551–9882	15.95	1.1	−23.55 ± 0.12	highmarsh	<1	Aa, Ea, Pg	*Gyraulus albus*	HAT – MHW	1.57 ± 0.42	−25.12 ± 0.44	0.12	0.29 ± 0.10	1.9 ± 0.2	−22.81 ± 0.49

Foraminifera abbreviation: Ab, *Ammonia beccarii* vars.; Cs, *Cribrononion subincertum*; Em, *Elphidium magellanicum*; Ea, *Elphidium advenum*; Na, *Nonionella auricula*. Ng, *Nonion glabrum*, Pg *Protelphidium granosum*; Ag, *Astrononion glabrum.* Detailed information on the SLIPs, including spatiotemporal data and uncertainties, bounding sedimentary facies, post-depositional corrections, and corrected RSL values, is provided in the Appendix (Supplementary Table).

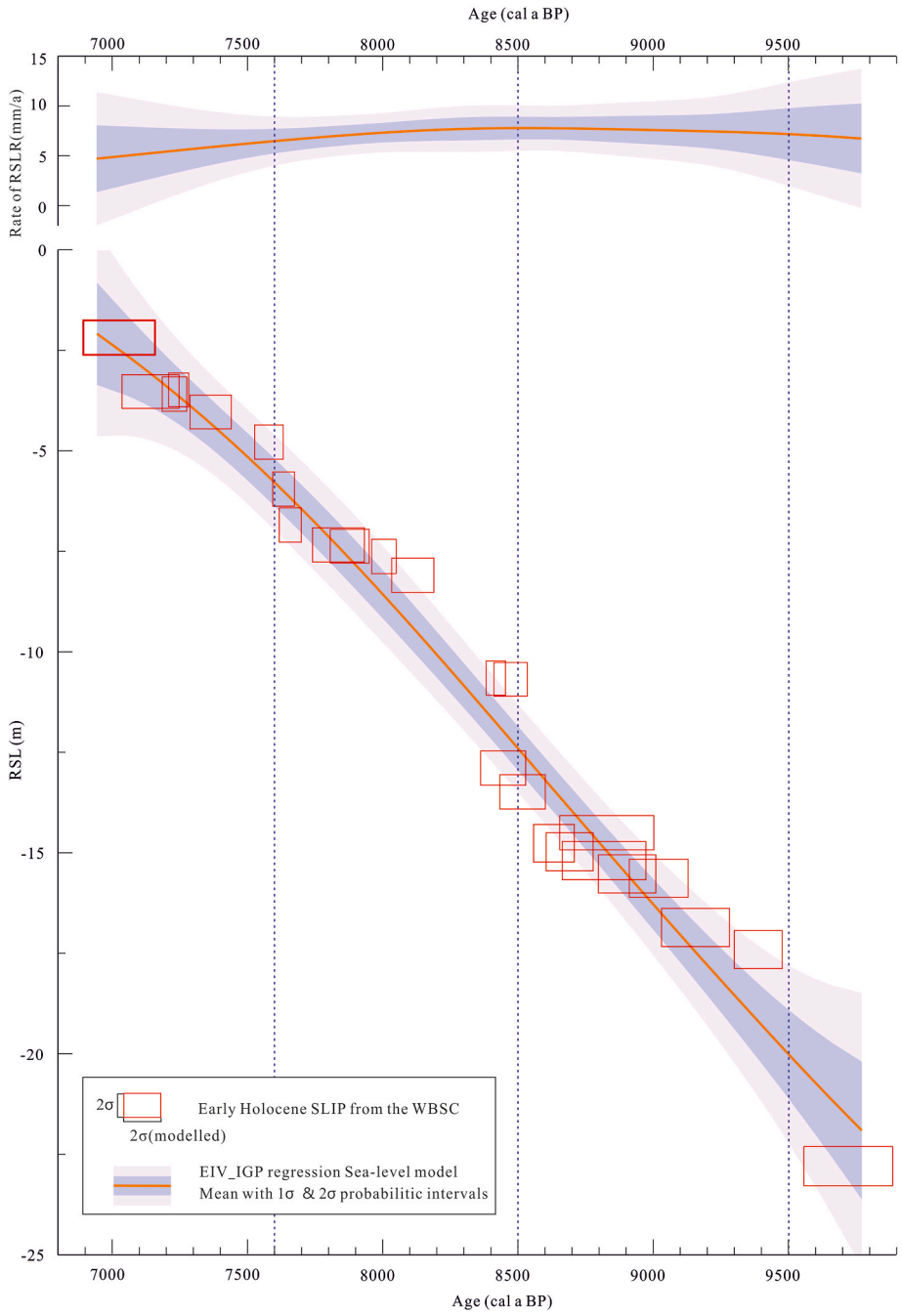

Fig. 3. The upper panel shows the rates of RSL change calculated through the EIV_IGP regression sea-level model. The lower panel indicates the elevations of the SLIPs and the modelled RSL change. The tectonic, sediment compaction and land subsidence factors have been corrected. Detailed data for SLIPs are available in Table 4.

(1σ), based on SLIP Qx03-3.

The six SLIPs (IDs: Qk11-1, Zw15-3, Tp23-1, Cz66-4, Cz65-3, and Qx03-3) document a sudden RSL rise of 6.67 ± 0.63 m, from −14.77 ± 0.47 to −8.11 ± 0.42 m MSL, during ~8500–8100 cal a BP. Notably, five SLIPs (Qk11-1, Zw15-3, Tp23-1, Cz66-4, and Cz65-3) indicate nearly simultaneous coastal flooding across tens of kilometers, occurring within the narrow timeframe of 8505 ± 135 cal a BP (1σ) and corresponding to an RSLR of 4.11 ± 0.63 m. This RSL jump recorded in the WBSC during ~8500–8100 cal a BP was associated with the 8.2 ka ice-melting event, driven by the complex drainage dynamics of Lake Agassiz-Ojibway (LAO) and the resulting meltwater pulse (Barber et al., 1999; Törnqvist and Hijma, 2012; Carlson and Clark, 2012).

As highlighted by Hijma and Cohen (2010, 2019), estimating the magnitude of a sea-level jump requires determining background RSLR rates from periods preceding and following the event. The RSLR rates derived from the EIV-IPG model outputs tend to exhibit a smoothed signal, meaning that fluctuations are attenuated. This is evident in the relatively consistent RSLR rates observed between 9000 and 8000 cal a BP, with only a subtle increase around 8500–8200 cal a BP. Consequently, using RSLR rates from the EIV-IPG model to establish background rates provides a conservative estimate of the jump magnitude. To determine these background rates, we selected two periods of slow sea-level rise before and after the jump, centered around 8600 and 7700 cal a BP, respectively, with rates of 7.8 ± 1.1 and 6.7 ± 1.1 mm/a (1σ). The resulting average background rate, 7.25 ± 0.78 mm/a, is comparable to the numerically predicted GIA-driven sea-level change of ~7.5

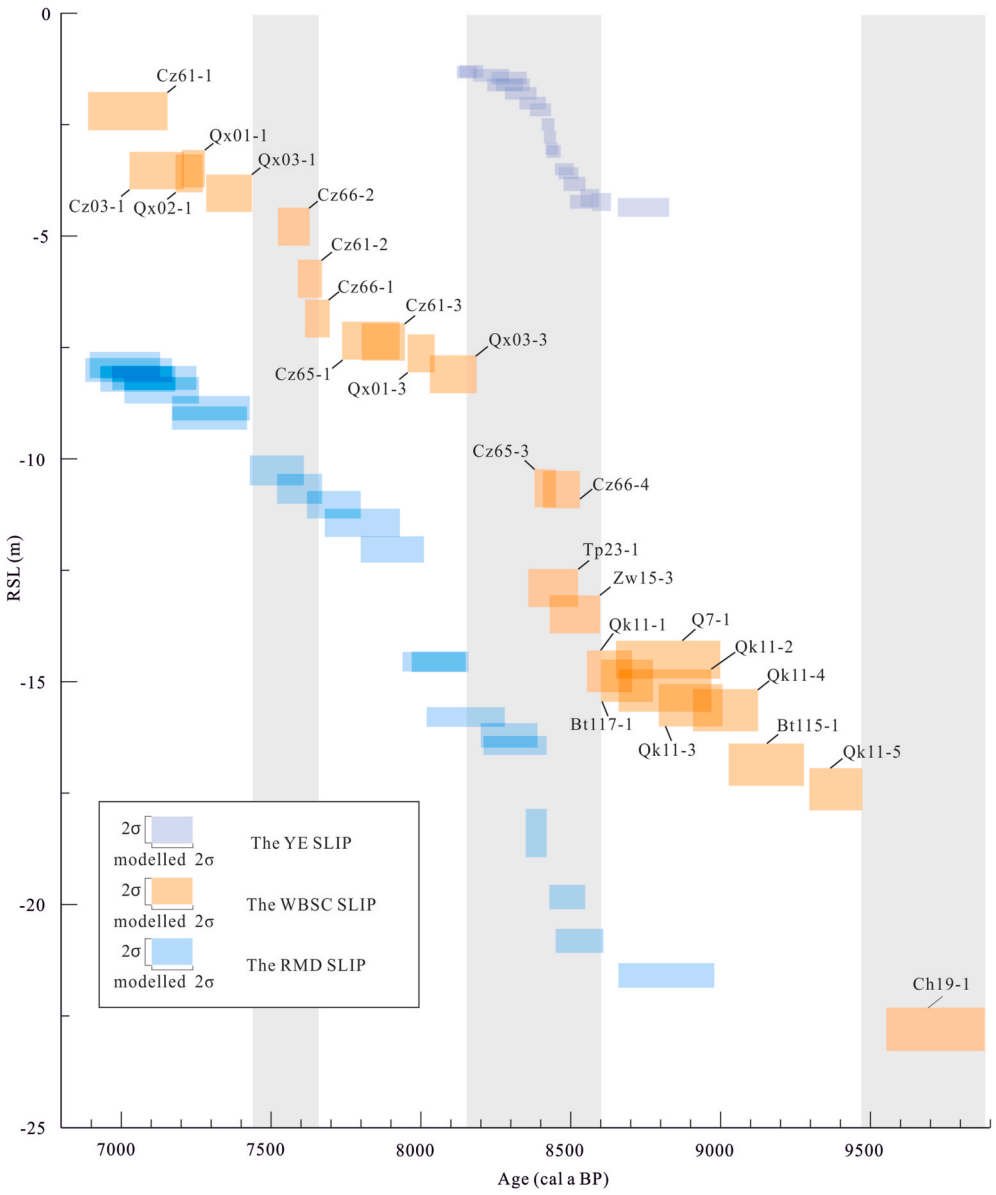

Fig. 4. Early Holocene RSL records for the WBSC and its comparisons from the Netherlands RMD (Hijma and Cohen, 2019) and the Scotland Ythan Estuary (YE) (Rush et al., 2023). Grey bars denote three periods of rapid of RSLR.

mm/a along Asian coasts over the interval from 9.0 to 8.5 ka (i.e., before the onset of the 8.2 ka event) (Kendall et al., 2008). Using this framework above, the total sea-level jump of this event was calculated to be 2.92 ± 0.93 m, with at least 2.55 ± 0.69 m occurring in the first phase.

Our reconstruction is consistent with works from the near-field such as the Netherlands RMD (Hijma and Cohen, 2019) and the Scotland Ythan Estuary (YE) (Rush et al., 2023). These two works, using a large number of SLIPs derived from peat across a broad geographical area, are also highly comparable to the reconstruction and magnitude analysis in this study. The three studies reveal a two-phased rise with different local magnitudes, all marked by rapid rates at the beginning (Table 5, Fig. 4).

The meltwater of the catastrophic drainage LAO caused a GMSL rise of ~0.5m during 1σ range of 8740–8160 cal a BP (Leverington et al., 2002; Teller et al., 2002). The total far field magnitude of this event is therefore very likely to be greater than the potential rise resulting from drainage of LAO. Due to the complete decay of the Eurasian Ice Sheets by ~9.7 ka BP (Stroeven et al., 2016), additional major sources for this meltwater event are likely to lie in the AIS, the Greenland Ice Sheet (GrIS), or the remaining sectors of the LIS such as the Hudson Bay Ice

Table 5
The timings and local magnitudes of first phase and total MWP associated with 8.2 ka cooling event in the far-field (WBSC) and near-fields (RMD and YE), along with their magnitude ratios relative to the far-field WBSC.

Event phase	Timing	Local magnitude (1σ)	Magnitude ratio to far-field WBSC
WBSC^{1st}	~8.50–8.40 cal ka	2.55 ± 0.69 m	–
WBSC ^{tot}	~8.50–8.10 cal ka	2.92 ± 0.93 m	–
YE ^{1st}	~8.55–8.40 cal ka	1.60 ± 0.57 m	0.63 ± 0.28
YE ^{tot}	~8.55–8.25 cal ka	1.91 ± 0.66 m	0.65 ± 0.30
RMD^{1st}	~8.45–8.30 cal ka	1.70 ± 0.60 m	0.67 ± 0.30
RMD ^{tot}	~8.45–8.20 cal ka	2.11 ± 0.89 m	0.72 ± 0.38

Saddle (HBIS) and the domes of Labrador and Keewatin.

The near-field (YE & RMD) to far-field (WBSC) sea-level jump ratio is calculated as 0.78 ± 0.16 based on the 8.2 ka LAO fingerprint model (c.f. Kendall et al., 2008). If the Hudson Bay and Hudson Strait components were rapidly melted during this event, the simulated fingerprint was very similar to the pattern of the LAO discharge, exhibiting only slightly northward shifts in the contours (Kendall et al., 2008). In contrast, substantial inputs from outside the LIS region, such as the Antarctic Ice Sheet (AIS) or Greenland Ice Sheet (GrIS), would alter the fingerprint pattern and consequently modify this ratio. Therefore, comparing observed near-field to far-field jump ratios with the predicted LAO fingerprint ratio may provide valuable insights into the sources of meltwater input.

The observed sea-level jump ratios are 0.63 ± 0.28 and 0.65 ± 0.30 for YE to WBSC, and 0.67 ± 0.30 and 0.72 ± 0.38 for RMD to WBSC, corresponding to the first phase and total MWP of the 8.2 ka event (Table 5). All these values are slightly lower than the 0.78 ± 0.16 predicted by the LAO fingerprint model, indicating limited contributions from either the AIS or GrIS. This suggests that the primary meltwater sources remained concentrated in the LIS, with significant contributions from ice sources outside the LAO region, likely directed toward Scotland and the Netherlands. A plausible contributor could involve the collapse of the HBIS, which are estimated to have stored 1.25 m (e.g., Ullman et al., 2016; Lochte et al., 2019) or 2.5 m equivalent global sea-level rise (e.g., Gregoire et al., 2012). In addition, it is not possible to rule out uncertain contributions from other LIS ice domes such as Labrador and Keewatin during this event.

5.3. MWP around 7600 cal a BP

Around 7600 cal a BP, the entire inland depositional condition underwent a subtle shift, transitioning from alternating supratidal and coastal plain context to a more established supratidal zone. This change is evidenced by an increased abundance of foraminifera upwards around 7600 cal a BP in cores Qx01, Qx02, Cz61, Cz65, and Cz66 (Fig. 2). In the most landward core Qx01, a plant sample (Qx01-2) from coastal plain directly beneath the more established supratidal sediments, yielded an age of 7794–7925 cal a BP (1σ), representing the maximum onset of this jump. Further seaward, in core Cz66, a peaty sample (Cz66-2) within the supratidal deposits, ~0.5 m above the last coastal plain unit, yielded an age of 7627–7671 cal a BP (1σ), indicating the minimum onset of the jump in this area. Within this onset window, we used the earliest SLIP, Cz66-2 (7627–7671 cal a BP, 1σ), to estimate the magnitude of the sea-level jump. The endpoint was tentatively assigned to 7516–7594 cal a BP (1σ), based on SLIP Cz66-1.

The three SLIPs (IDs: Cz66-1, Cz66-2, and Cz61-1) indicate a rapid sea-level rise of 2.06 ± 0.57 m within a narrow age range of 7593 ± 78 cal a BP (1σ). Two of these SLIPs, used to calculate its magnitude, were derived from the same sampling core (Cz66), enabling uncertainties related to local signals, such as tectonic deformation and land subsidence, to be safely omitted.

The smoothed RSLR rates derived from the EIV-IPG model during the relatively slow-rise periods before and after the jump, around 7700 and 7300 cal a BP, were 6.7 ± 1.1 and 5.7 ± 2.0 mm/a (1σ), respectively. Therefore, an average rate of 6.47 ± 0.96 mm/a is taken as the background rate. Accounting for the background RSL rise rates during time interval, the additional rise of this jump is reduced to 1.45 ± 0.64 m.

Along the Netherlands coast, however, the RMD sea-level database shows a steadily decreasing RSLR rate, excludes a meter-scale RSLR acceleration around 7.6 ka BP, and suggests that the absence of SLIPs around 7.4 ka BP reflects either increased RSLR rates or limited sampling (Fig. 4) (Hijma and Cohen, 2019). This clear discrepancy points to the fingerprint ratio of the Northern Hemisphere ice sheets as the primary source. In particular, the LIS is identified as a significant contributor to sea-level rise during this period, as Carlson et al. (2008) suggest, with LIS chronology and Labrador Sea $\delta^{18}O$ records showing a deceleration of retreat between ~8.5 and 7.6 ka BP, followed by an accelerated retreat in the Labrador sector from ~7.6 to 6.8 ka BP, contributing approximately 7 mm/a to GMSL rise.

6. Conclusions

Through the analysis of sediments, microfossil foraminifera, and radiocarbon dating of 14 cores from the WBSC, we generated a new dataset of 25 high-confidence early Holocene SLIPs from high marsh vegetation samples. The altitudes of these SLIPs were adjusted for self-compaction, long-term tectonic subsidence, and ground lowering due to water extraction, enabling the reconstruction of early Holocene RSL history and evaluation of far-field response to MWPs.

Between approximately 9800 and 6900 cal a BP, RSL rose rapidly from −22.81 ± 0.49 m to −2.20 ± 0.42 m. The rate of RSLR was particularly high before 8000 cal a BP, around 7–8 mm/a. After 8000 cal a BP, the rate rapidly decreased to 5.0 mm/a by 7000 cal a BP. Our analysis identified three distinct sea-level events occurring before 9500, ~8500, and ~7600 cal a BP.

1. The sea-level data from the WBSC suggests a RSLR of at least 5.4 ± 0.63 m occurring within the narrow timeframe of 9603 ± 288 cal a BP (1σ). This result aligns with a rapid sea-level rise event in the PRD region within a similar time interval and supports the occurrence of a sea-level acceleration before 9500 cal a BP from far-field Asian sites.
2. Our reconstructions suggest that the meltwater pulse leading up to the 8.2 ka climate event had a two-phase structure, marked by rapid rates at the beginning. On top of background RSLR, this MWP from ~8500 to 8100 cal a BP resulted in an additional RSLR of 2.92 ± 0.93 m, with 2.55 ± 0.69 m in the first phase at 8505 ± 135 cal a BP (1σ). The magnitude of the event in the far-field WBSC region indicates that the contribution from LAO was not sufficient to account for these meltwater pulses. Comparison with near-field sea-level records from the Netherlands RMD and the Scotland YE supports the collapse of the HBIS as the dominant source of the observed sea-level rise.
3. The final sea-level event in the early Holocene, shown as an instantaneous RSLR of 2.06 ± 0.57 m within a narrow age range of 7593 ± 78 cal a BP (1σ), represents a minor MWP with an additional RSLR of 1.45 ± 0.64 m. This far-field jump is significantly greater than the records from the near-field Netherlands RMD, which excludes a meter-scale RSLR acceleration around 7.6 ka BP. This clear discrepancy supports the LIS Labrador sector as a significant contributor to this event.

Author contributions

Lizhu Tian contributed to scientific question choice, design of field work including data analyses, results and discussion, paper writing and revising; Fu Wang contributed to part of sampling, measurements discussion and to revising part of the paper; Jianfen Li contributed to foraminifera data analysis; Bert L. Vermeersen and Hong Wang contributed to discussion.

Declaration of competing interest

The authors declare that they have no known competing financial interests or personal relationships that could have appeared to influence the work reported in this paper.

Acknowledgments

The study was supported for design and research by the Major Program of the National Science Foundation of China (42293261) and CGS Projects (DD20211301 and DD20230091).

Appendix A. Supplementary data

Supplementary data to this article can be found online at https://doi.org/10.1016/j.quascirev.2025.109430.

Data availability

All data and/or code is contained within the submission.

References

Allen, M.B., Macdonald, D.I.M., Xun, Z., Vincent, S.J., Brouet-Menzies, C., 1997. Early Cenozoic two-phase extension and late Cenozoic thermal subsidence and inversion of the Bohai Basin, northern China. Mar. Petrol. Geol. 14 (7–8), 951–972. https://doi.org/10.1016/S0264-8172(97)00027-5.

Barber, D.C., et al., 1999. Forcing of the cold event of 8,200 years ago by catastrophic drainage of Laurentide lakes. Nature 400, 344–348. https://doi.org/10.1038/22504.

Bard, E., et al., 1996. Deglacial sea-level record from Tahiti corals and the timing of global meltwater discharge. Nature 382, 241–244. https://doi.org/10.1038/382241a0.

Bard, E., Hamelin, B., Delanghe-Sabatier, D., 2010. Deglacial meltwater pulse 1B and younger dryas sea levels revisited with boreholes at tathiti. Nature 327, 1235–1237. https://doi.org/10.1038/nature08275.

Bird, M.I., Fifield, L.K., Teh, T.S., Chang, C.H., Shirlaw, N., Lambeck, K., 2007. An inflection in the rate of early mid-Holocene eustatic sea-level rise: a new sea-level curve from Singapore. Estuar. Coast Shelf Sci. 71, 523–536. https://doi.org/10.1016/j.ecss.2006.07.004.

Blanchon, P., Shaw, J., 1995. Reef drowning during the last deglaciation: evidence for catastrophic sea-level rise and ice-sheet collapse. Geology 23 (1), 4–8. https://doi.org/10.1130/0091-7613(1995)023<0004:RDDTLD>2.3.CO;2.

Bradley, S. L., Milne, G. A., Horton, B. P., Zong, Y., 2016. Modelling sea level data from China and Malay–Thailand to estimate Holocene ice-volume equivalent sea level change. Quat. Sci. Rev. 137, 54–68. https://doi.org/10.1016/j.quascirev.2016.02.002.

Bronk Ramsey, C., 2009. Bayesian analysis of radiocarbon dates. Radiocarbon 51 (1), 337–360. https://doi.org/10.2458/azu_js_rc.51.3494.

Cahill, N., Kemp, A.C., Horton, B.P., Parnell, A.C., 2015. Modeling sea-level change using errors-in-variables integrated Gaussian processes. Ann. Appl. Stat. 9 (2), 547–571. https://doi.org/10.1214/15-AOAS824.

Cahill, N., Kemp, A.C., Horton, B.P., Parnell, A.C., 2016. A Bayesian hierarchical model for reconstructing relative sea level: from raw data to rates of change. Clim. Past 12 (2), 525–542. https://doi.org/10.5194/cp-12-525-2016.

Carlson, A.E., Clark, P.U., 2012. Ice-sheet sources of sea-level rise and freshwater discharge during the last deglaciation. Rev. Geophys. 50 (4). https://doi.org/10.1029/2011RG000371.

Carlson, A.E., et al., 2008. Rapid early Holocene deglaciation of the Laurentide ice sheet. Nat. Geosci. 1, 620–624. https://doi.org/10.1038/ngeo285.

Chen, Q., Zhu, Y., 2012. Holocene evolution of bottom sediment distribution on the continental shelves of the Bohai Sea, Yellow Sea and East China Sea. Sediment. Geol. 273–274, 58–72. https://doi.org/10.1016/j.sedgeo.2012.06.011.

Clark, P.U., Marshall, S.J., Clarke, G.K.C., Hostetler, S.W., Licciardi, J.M., Teller, J.T., 2001. Freshwater forcing of abrupt climate change during the last glaciation. Science 293 (5528), 283–287. https://doi.org/10.1126/science.10625.

Cronin, T.M., et al., 2007. Rapid sea level rise and ice sheet response to 8200-year climate event. Geophys. Res. Lett. 34, L20603. https://doi.org/10.1029/2007GL031318.

Dalton, A.S., et al., 2020. An updated radiocarbon-based ice margin chronology for the last deglaciation of the North American Ice Sheet Complex. Quat. Sci. Rev. 234, 106223. https://doi.org/10.1016/j.quascirev.2020.106223.

DPA and NMDC, 1991. Analysis of marine environmental conditions in western Bohai Bay (Tide section). Dagang Petroleum Administration and National Marine Data Center.

Fairbanks, R.G., 1989. A 17,000-year glacio-eustatic sea level record: influence of glacial melting rates on the Younger Dryas event and deep-ocean circulation. Nature 342, 637–642. https://doi.org/10.1038/342637a0.

Gregoire, L.J., Payne, A.J., Valdes, P.J., 2012. Deglacial rapid sea level rises caused by ice-sheet saddle collapses. Nature 487, 219–222. https://doi.org/10.1038/nature11257.

Hanebuth, T., Stattegger, K., Grootes, P.M., 2000. Rapid flooding of the sunda shelf: a late-glacial sea-level record. Science 288, 1033–1035. https://doi.org/10.1126/science.288.5468.103.

Hijma, M.P., Cohen, K.M., 2010. Timing and magnitude of the sea-level jump preluding the 8200 yr event. Geology 38 (1), 275–278. https://doi.org/10.1130/G30439.

Hijma, M.P., Cohen, K.M., 2019. Holocene sea-level database for the Rhine-Meuse Delta, The Netherlands: implications for the pre-8.2 ka sea-level jump. Quat. Sci. Rev. 214, 68–86. https://doi.org/10.1016/j.quascirev.2019.05.001.

Hijma, M.P., Engelhart, S.E., Törnqvist, T.E., Horton, B.P., Hu, P., Hill, D.F., 2015. A Protocol for a Geological Sea-Level Database, Handbook of Sea-Level Research. John Wiley & Sons, Ltd, pp. 536–553. https://doi.org/10.1002/9781118452547.ch34.

Hu, S., O'Sullivan, P.B., Raza, A., Kohn, B.P., 2001. Thermal history and tectonic subsidence of the Bohai Basin, northern China: a Cenozoic rifted and local pull-apart basin. Phys. Earth Planet. Inter. 126 (3–4), 221–235. https://doi.org/10.1016/S0031-9201(01)00257-6.

Jones, R.S., et al., 2022. Stability of the antarctic ice sheet during the pre-industrial Holocene. Nat. Rev. Earth Environ. 3 (8), 500–515. https://doi.org/10.1038/s43017-022-00309-5.

Kendall, R.A., Mitrovica, J.X., Milne, G.A., Tornqvist, T.E., Li, Y., 2008. The sea-level fingerprint of the 8.2 ka climate event. Geology 36 (5), 423–426. https://doi.org/10.1130/G24550A.1.

Khan, N.S., et al., 2019. Inception of a global atlas of sea levels since the Last Glacial Maximum. Quat. Sci. Rev. 220, 359–371. https://doi.org/10.1016/j.quascirev.2019.07.0160277-3791.

Lajeunesse, P., St-Onge, G., 2008. The subglacial origin of the Lake Agassiz-Ojibway final outburst flood. Nat. Geosci. 1, 184–188. https://doi.org/10.1038/ngeo130.

Leverington, D.W., Mann, J.D., Teller, J.T., 2002. Changes in the bathymetry and volume of glacial Lake Agassiz between 9200 and 7700 14C yr BP. Quaternary Research 57, 244–252. https://doi.org/10.1006/qres.2001.2311.

Li, J., et al., 2021. Holocene sea level trend on the west coast of Bohai Bay, China: reanalysis and standardization. Acta Oceanol. Sin. 40 (7), 198–248. https://doi.org/10.1007/s13131-021-1730-5.

Li, J., et al., 2010. Modern foraminifera assemblages: vertical zonation and its indication for Holocene sea level and geoenvironmental reconstruction in Bohai Bay, China. Geol. Bull. China 29 (5), 650–659. https://doi.org/10.3969/j.issn.1671-2552.2010.05.003 (in Chinese with English abstract).

Li, Y.X., Törnqvist, T.E., Nevitt, J.M., Kohl, B., 2012. Synchronizing a sea-level jump, final Lake Agassiz drainage, and abrupt cooling 8200 years ago. Earth Planet Sci. Lett. 315, 41–50. https://doi.org/10.1016/j.epsl.2011.05.034.

Li, J., et al., 2016. Sea-level indicated by foraminifera assemblages living in the open muddy flats with or without influence of the chenier ridges in Bohai Bay coastal areas. Geol. Bull. China 35 (10), 1578–1583. https://doi.org/10.3969/j.issn.1671-2552.2016.10.003 (in Chinese with English abstract).

Liu, J.P., Milliman, J.D., Gao, S., Cheng, P., 2004. Holocene development of the Yellow River's subaqueous delta, North Yellow sea. Mar. Geol. 209, 45–67. https://doi.org/10.1016/j.margeo.2004.06.009.

Liu, J., Saito, Y., Wang, H., Yang, Z., Nakashima, R., 2007. Sedimentary evolution of the Holocene subaqueous clinoform off the shandong peninsula in the Yellow Sea. Mar. Geol. 236, 165–187. https://doi.org/10.1016/j.margeo.2006.10.031.

Liu, Q., He, L., Huang, F., Zhang, L., 2016. Cenozoic lithospheric evolution of the Bohai bay basin, eastern North China craton constraint from tectono-thermal modeling. J. Asian Earth Sci. 115, 368–382. https://doi.org/10.1016/j.jog.2016.09.005.

Liu, Q., He, L., Yi, Z., Zhang, L., 2022. Anomalous post-rift subsidence in the Bohai Bay Basin, Eastern China: contributions from mantle process and fault activity. Tectonics 41 (1), e2021TC006748. https://doi.org/10.1029/2021TC006748.

Lochte, A.A., et al., 2019. Labrador Sea freshening at 8.5 ka BP caused by Hudson Bay ice saddle collapse. Nat. Commun. 10, 1–9. https://doi.org/10.1038/s41467-019-08408-6.

Nichols, K.A., Goehring, B.M., Balco, G., Johnson, J.S., Hein, A.S., Todd, C., 2019. New last glacial maximum ice thickness constraints for the Weddell Sea Embayment, Antarctica. Cryosphere 13 (11), 2935–2951. https://doi.org/10.5194/tc-13-2935-2019.

Pirazzoli, P.A., 1991. World Atlas of Holocene Sea-Level Changes. Elsevier, Amsterdam.

Qin, Y., Zhao, Y., Chen, L., Zhao, S., 1990. Geology of the Bohai Sea. Science Press, Beijing.

Reimer, P.J., et al., 2020. The IntCal20 Northern Hemisphere radiocarbon age calibration curve (0–55 cal kBP). Radiocarbon 62, 725–757. https://doi.org/10.1017/RDC.2020.41.

Rush, G., et al., 2023. The magnitude and source of meltwater forcing of the 8.2 ka climate event constrained by relative sea-level data from eastern Scotland. Quaternary Science Advances 12, 100119. https://doi.org/10.1016/j.qsa.2023.100119.

Shennan, I., Innes, J.B., Long, A.J., Zong, Y., 1995. Holocene relative sea-level changes and coastal vegetation history at Kentra Moss, Argyll, northwest Scotland. Mar. Geol. 124, 43–59. https://doi.org/10.1016/0025-3227(95)00031-S.

Smith, D.E., Harrison, S., Firth, C.R., Jordan, J.T., 2011. The early Holocene sea level rise. Quat. Sci. Rev. 30 (15–16), 1846–1860. https://doi.org/10.1016/j.quascirev.2011.04.019.

Spector, P., Stone, J., Cowdery, S.G., Hall, B., Conway, H., Bromley, G., 2017. Rapid early-holocene deglaciation in the Ross Sea, Antarctica. Geophys. Res. Lett. 44 (15), 7817–7825. https://doi.org/10.1002/2017GL074216.

Stroeven, A.P., et al., 2016. Deglaciation of fennoscandia. Quat. Sci. Rev. 147, 91–121. https://doi.org/10.1016/j.quascirev.2015.09.016.

Su, G., Wu, Y., Zhan, W., Zheng, Z., Chang, L., Wang, J., 2021. Spatiotemporal evolution characteristics of land subsidence caused by groundwater depletion in the North China plain during the past six decades. J. Hydrol. 600, 126678. https://doi.org/10.1016/j.jhydrol.2021.126678.

Teller, J.T., Leverington, D.W., Mann, J.D., 2002. Freshwater outbursts to the oceans from glacial Lake Agassiz and their role in climate change during the last deglaciation. Quat. Sci. Rev. 21, 879–887. https://doi.org/10.1016/S0277-3791(01)00145-7.

Tian, L., et al., 2017. Post-glacial sequence and sedimentation in the western Bohai Sea, China, and its linkage to global sea-level changes. Mar. Geol. 388, 12–24. https://doi.org/10.1016/j.margeo.2017.04.003.

Tjallingii, R., Stattegger, K., Wetzel, A., Van Phach, P., 2010. Infilling and flooding of the Mekong River incised valley during deglacial sea-level rise. Quat. Sci. Rev. 29 (11), 1432–1444. https://doi.org/10.1016/j.quascirev.2010.02.022.

Törnqvist, T.E., Hijma, M.P., 2012. Links between early Holocene ice-sheet decay, sea-level rise and abrupt climate change. Nat. Geosci. 5, 601. https://doi.org/10.1038/ngeo1536.

Törnqvist, T.E., Bick, S.J., Gonzalez, J.L., van der Borg, K., de Jong, A.F.M., 2004. Tracking the sea-level signature of the 8.2ka cooling event: new constraints from the Mississippi delta. Geophys. Res. Lett. 31, L23309. https://doi.org/10.1029/2004GL021429.

Uehara, K., Saito, Y., 2003. Late Quaternary evolution of the Yellow/East China Sea tidal regime and its impacts on sediments dispersal and seafloor morphology. Sediment. Geol. 162, 25–38. https://doi.org/10.1016/S0037-0738(03)00234-3.

Ullman, D.J., et al., 2016. Final Laurentide ice-sheet deglaciation and Holocene climate-sea level change. Quat. Sci. Rev. 152, 49–59. https://doi.org/10.1016/j.quascirev.2016.09.014.

Wang, Z., et al., 2010. Lithological and palynological evidence of late Quaternary depositional environments in the subaqueous Yangtze delta, China. Quaternary Research 73, 550–562. https://doi.org/10.1016/j.yqres.2009.11.001.

Wang, Z., et al., 2013. Early to mid-Holocene rapid sea-level rise and coastal response on the southern Yangtze delta plain, China. J. Quat. Sci. 28 (7), 659–672. https://doi.org/10.1002/jqs.2657.

Wang, F., et al., 2015. The record of mid-Holocene maximum landward marine transgression in the west coast of Bohai Bay, China. Mar. Geol. 359, 89–95. https://doi.org/10.1016/j.margeo.2014.11.013.

Wang, F., et al., 2020a. Holocene sea-level change on the central coast of Bohai Bay, China. Earth Surf. Dyn. 8, 679–693. https://doi.org/10.5194/esurf-8-679-2020.

Wang, S., Ge, J., Kilbourne, K.H., Wang, Z., 2020b. Numerical simulation of mid Holocene tidal regime and storm-tide inundation in the south Yangtze coastal plain, East China. Mar. Geol. 423, 106134. https://doi.org/10.1016/j.margeo.2020.106134.

Wang, F., et al., 2024. Sea level change in Bohai bay. North China Geology 47 (1), 1–20. https://doi.org/10.19948/j.12-1471/P.2024.01.01 (in Chinese with English abstract).

Xiong, H., Zong, Y., Qian, P., Huang, G., Fu, S., 2018. Holocene sea-level history of the northern coast of South China Sea. Quat. Sci. Rev. 194, 12–26. https://doi.org/10.1016/j.quascirev.2018.06.002.

Xue, C., 1993. Historical changes in the Yellow River delta, China. Mar. Geol. 113, 321–329. https://doi.org/10.1016/0025-3227(93)90025-Q.

Yao, Z., et al., 2017. Sedimentary environment and paleo-tidal evolution of the eastern Bohai Sea, China since the last glaciation. Quat. Int. 440, 129–138. https://doi.org/10.1016/j.quaint.2016.04.010.

Yu, S.-Y., Berglund, B.E., Sandgren, P., Lambeck, K., 2007. Evidence for a rapid sea-level rise 7600 yr. ago. Geology 35, 891–894. https://doi.org/10.1130/G23859A.1.